Dalton Transactions

ROYAL SOCIETY OF CHEMISTRY

PAPER

View Article Online
View Journal | View Issue

Cite this: *Dalton Trans.*, 2026, **55**, 3375

Cationic heteroleptic Ni(II) complexes of dithiocarbamate and phosphine ligands: synthesis, characterization and proton reduction study

Sarvesh Kumar Pal, †[a] Anjali Mishra, †[a] Gaurav Kumar Mishra, [b] Ruben Hansson,[c] Vishal Jaiswal,[d] Ebbe Nordlander, [c] George Lisensky, [e] Amrendra Kumar Singh, [d] Nanhai Singh,[a] Prem Lama *[f] and Kamlesh Kumar *[a]

Three cationic heteroleptic Ni(II) dithiocarbamate complexes ($[Ni(L)(L')_n]PF_6$, n = 1 or 2) were synthesized and characterized to explore the relationship between diphosphine chelate ring size and their electrocatalytic activity for hydrogen production. These complexes (**1–3**) feature a common dithiocarbamate ligand (L) and varied diphosphine ligands (L'): dppm (**1**), dppe (**2**), and dppp (**3**). Single-crystal X-ray analysis showed a distorted square pyramidal geometry for **1** and square planar geometries for **2** and **3** around the NiP_2S_2 core. Electrochemical studies revealed a small variation in redox potentials ($\Delta E_{1/2} \approx 60$ mV), suggesting a weak electronic effect of ligands from dppm (**1**) to dppp (**3**). However, a significant difference in catalytic half-wave potentials ($\Delta E_{cat/2} \approx 200$ mV in 4 mM CH_3COOH) indicates a strong influence of the P–Ni–P bite angles. The catalytic activity of the complexes is significantly influenced by the chelate ring size and their P–Ni–P bite angles, which follow the trend 92.07(4)° (**3**) > 86.84(6)° (**2**) > 75.24(3)° (**1**). The enhanced electrocatalytic performance of **3** with a low overpotential (~600 mV), a high turnover frequency (~706 s^{-1}), and faradaic efficiency (88%) is attributed to the conformational flexibility of the six-membered chelate ring in **3** due to the dppp ligand. Both experimental data and DFT calculations support an ECEC mechanism for the HER catalysed by heteroleptic Ni(II) complexes with the formation of Ni(III)–H intermediate species.

Received 27th November 2025,
Accepted 19th January 2026

DOI: 10.1039/d5dt02840j

rsc.li/dalton

Introduction

Extensive research has focused on finding alternative, eco-friendly fuel sources to reduce dependence on fossil fuels for energy. In this regard, generating molecular hydrogen (H_2) gas as a carbon-free fuel through water splitting has attracted significant attention.[1–3] This process oxidizes water to produce O_2 and reduces protons to produce H_2.[4] Early investigations indicate that noble metals like Pt and Ru can act as catalysts for both electrocatalytic and photocatalytic reduction of protons, resulting in the production of H_2. However, their large-scale applications are limited due to high cost and low availability.[5] Therefore, researchers have dedicated significant efforts to develop cost-effective catalysts containing Earth-abundant transition metals. Metal complexes of 3d transition metals such as Fe,[6,7] Co,[8–10] Cu,[11,12] Mn,[13] *etc.*, exhibit potential application as electrocatalysts for the hydrogen evolution reaction (HER) under both homogeneous and heterogeneous conditions.

Nickel-based molecular HER catalysts have attracted attention in recent years due to their tunable redox properties influenced by the electronic, steric, and chelating effects of ligands surrounding the metal centre.[14–19] Incorporating a pendant amine functionality in nickel phosphine complexes notably enhances their catalytic hydrogen production.[20,21] Such nickel catalysts exhibit remarkable efficiencies, achieving high turnover frequencies for H_2 production even in acetonitrile solutions containing water. Recent progress in square planar Ni-based HER catalysts emphasizes ligand design to enhance the electrocatalytic activity and the catalyst stability.[22,23] Modern systems employ redox-active or proton-responsive

[a]*Department of Chemistry, Institute of Science, Banaras Hindu University, Varanasi-221005, India. E-mail: kamlesh.kumar@bhu.ac.in*
[b]*Department of Chemistry, University of Delhi, Delhi-110007, India*
[c]*Chemical Physics, Department of Chemistry, Lund University, P.O. Box 124, SE-22100 Lund, Sweden*
[d]*Department of Chemistry, Indian Institute of Technology Indore, Simrol, Indore 453552, M.P., India*
[e]*Department of Chemistry, Beloit College, 700 College St., Beloit, WI 53511, USA*
[f]*CSIR-Indian Institute of Petroleum, Nanocatalysis Area, LSP Division, Mohkampur, Dehradun-248005, India. E-mail: prem.lama@iip.res.in*
† Equal contribution.

ligands that facilitate the formation of intermediate Ni(III)–H, which results in enhanced hydrogen production under homogeneous conditions.[24] DuBois and co-workers have described a proficient Ni catalyst with cyclic diphosphine ligands forming seven-membered chelate rings, providing the necessary flexibility for electrocatalytic proton reduction.[25]

The use of transition metal complexes containing dithiocarbamate and diphosphine ligands as molecular electrocatalysts under homogeneous conditions is rare. Despite extensive studies of the coordination chemistry of dithiolato complexes, there are only a few reports that describe electrocatalytic proton reduction based on such complexes.[17,19,26,27] In one such report, Fan *et al.* have synthesized thiolato-bridged cyclopentadienyl dimer complexes, which have been identified as efficient and durable proton reduction electrocatalysts when utilizing acetic acid as a proton source.[19,27,28] The same group also reported dimeric nickel complexes featuring two bridging thiolato ligands, which exhibited catalytic activity upon electrochemical reduction. These complexes demonstrated efficient homogeneous proton reduction, achieving notable rate constants (k_{obs}) of approximately 10^4 s^{-1} at moderate overpotentials ranging from 0.5 to 0.6 V.[17] The Ni(II) complex [Ni(bdt)(dppf)] (where bdt = 1,2-benzenedithiolate and dppf = 1,1′-bis(diphenylphosphino)ferrocene) reported by Jones *et al.* demonstrates rapid and efficient performance for hydrogen production.[29] However, a similar compound, [Ni(bdt)(dppe)], where dppe = 1,2-bis(diphenylphosphino)ethane, was not found to be efficient for the hydrogen evolution reaction (HER). Zhang *et al.*[30] synthesized NiS_2P_2 based square planar complexes and investigated the electrocatalytic hydrogen evolution using trifluoroacetic acid as a proton source. The variation of the substituent from electron donating to withdrawing groups does not substantially affect the HER overpotential (~1 V) and TOF (~800 s^{-1}). These experimental results suggest that the chelate ring size (and associated ring strain) may be the governing factor in proton reduction by NiP_2S_2-based complexes.

Recently, we highlighted the influence of rigidity and the chelation effect on proton reduction by heteroleptic [Ni(II)1,1-dithiolate-phosphine] complexes, containing phosphine ligands 1,2-bis(diphenylphosphino)ethane (dppe), 1,1-bis(diphenylphosphino)ferrocene (dppf), and triphenylphosphine (PPh_3). We observed that the flexibility of the monodentate PPh_3 ligand favors the easy formation of a transition state and, therefore, results in enhanced electrocatalytic activity.[18] The comparatively lower electrocatalytic activity of the Ni(II) complex containing the bidentate dppe ligand was attributed to high ring strain and reduced flexibility of the 5-membered chelate ring.

It has been shown that polydentate ligands play pivotal roles in stabilizing coordination complexes *via* the chelate ring size around the metal center. The chelate ring size regulates the stability, electronic properties, kinetics, and ion selectivity of the complexes.[31,32] Smaller chelate rings exhibit more ring strain and are usually less flexible, while larger chelate rings offer greater flexibility with reduced strain. The current interest lies in investigating how the chelate ring size in NiP_2S_2-based complexes influences electrocatalytic proton reduction.

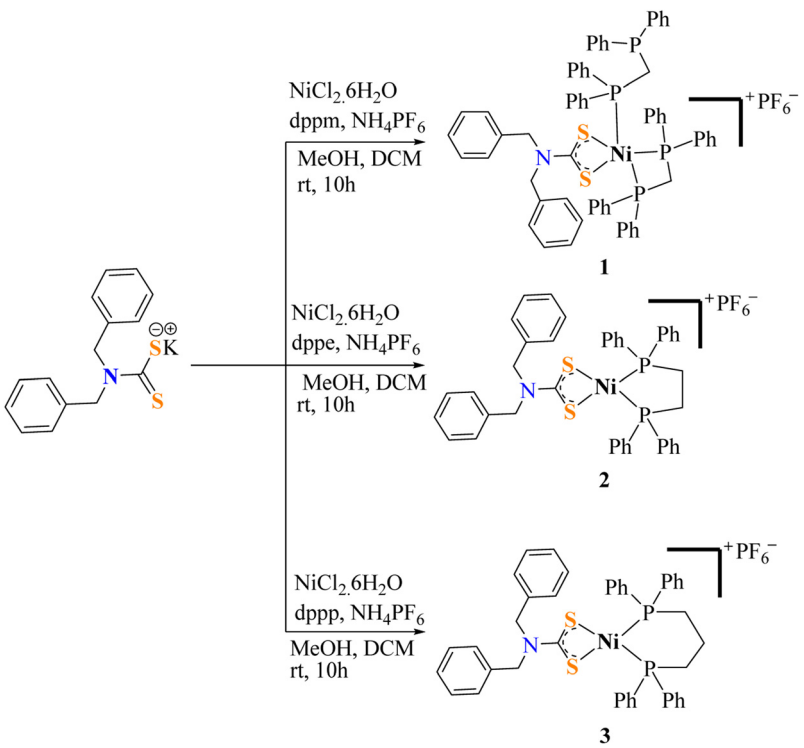

Scheme 1 Synthesis of nickel complexes **1–3**.

In this study, we have synthesized cationic heteroleptic Ni(II) complexes (**1–3**) containing benzyl functionalized dithiocarbamate and diphosphine ligands such as 1,1-bis(diphenylphosphino)methane (dppm), 1,2-bis(diphenylphosphino)ethane (dppe), and 1,3-bis(diphenylphosphino)propane (dppp), as shown in Scheme 1. This study highlights the importance of dithiocarbamate and diphosphine ligands in heteroleptic Ni(II) complexes for the HER. The flexible chelate ring in the diphosphine ligand system was employed to investigate its structural adaptability and proton delivery efficiency, which may contribute to the overall enhanced reactivity and stability of Ni(II) complexes. Furthermore, we have investigated the electrochemical redox and electrocatalytic properties of the new complexes toward the electrochemical HER using acetic acid as a proton source in a non-aqueous medium. We have also examined the electronic and chelate ring size effects of the coordinated diphosphine ligands on the HER activity. Finally, computational and spectroelectrochemical studies were conducted to gain mechanistic insights into electrocatalytic proton reduction.

Results and discussion

Synthesis and characterization of ligands and complexes

The potassium salt of the dithiocarbamate ligand was synthesized following previously reported procedures[33–35] and was fully characterized by FT-IR and NMR spectroscopic techniques. The spectral data were in good agreement with reported values. Cationic heteroleptic nickel complexes were synthesized *in situ*, where methanol solutions of $NiCl_2{\cdot}6H_2O$ and the dithiocarbamate ligand were added simultaneously to a dichloromethane solution of the relevant diphosphine ligand (dppm, dppe, or dppp). After the addition of dithiocarbamate solution, one equivalent of solid NH_4PF_6 was added to the reaction flask (Scheme 1). Complex **1** was obtained as brown solid whereas, complexes **2**, and **3** were obtained as reddish-orange solids. These complexes are stable to air and moisture and melt in the temperature range of 160–245 °C. The details of physical properties for all complexes are given in Table 1. Furthermore, the complexes were fully characterized by FT-IR, ^{1}H, $^{13}C\{^1H\}$, $^{31}P\{^1H\}$, and ^{19}F NMR, UV-Vis spectroscopy techniques. The solid-state structures of complexes **1** and **3** have also been elucidated by single-crystal X-ray diffraction (*vide infra*).

UV-visible absorption spectral studies

The UV-Vis absorption spectra of cationic heteroleptic complexes **1–3** were recorded in dichloromethane solution at room temperature with a concentration of 10^{-5} M, as shown in Fig. 1. The absorption bands of the complexes show an intense absorption band at ~306 to 310 nm (ε = ~0.63–0.81 × 10^5 M^{-1} cm^{-1}), which may be assigned to inter-/intra ligand charge transfer (ILCT) transitions due to the coordinated dithiocarbamate/diphosphine ligands in the complexes.[34,36] In complexes **1–3**, a weak absorption band appeared at ~397 to 445 nm (ε = ~1.24–0.85 × 10^3 $M^{-1}cm^{-1}$), which was assigned to metal-to-ligand charge transfer (MLCT) transitions (Fig. 1).[18,29,37]

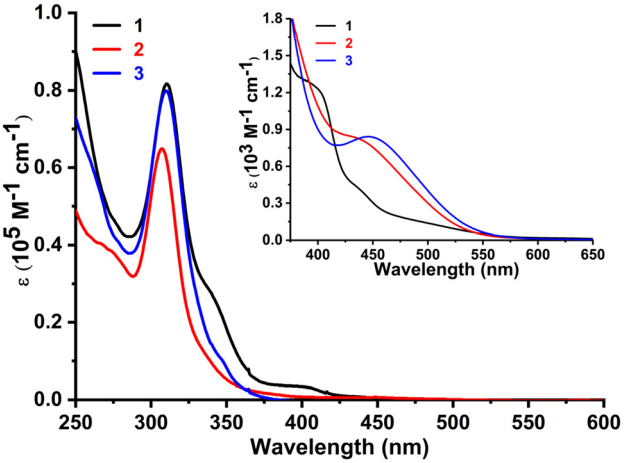

Fig. 1 UV-Vis spectra of 10^{-5} M and 10^{-3} M (inset figure) solutions of complexes **1–3** in dichloromethane.

IR and NMR spectral studies

The IR spectra of complexes **1–3** showed bands at 1497–1516 cm^{-1} for ν_{C-N} and 1002–1024 cm^{-1} for ν_{C-S} vibrations, respectively, which are distinctive for dithiocarbamate ligand coordination.[38] The increase in the ν_{C-N} frequency in the complexes, relative to the uncoordinated ligand (ν_{C-N} = 1421 cm^{-1}),[34,39] can be ascribed to the π delocalization of the nitrogen lone pair electrons across the NCS_2 backbone.[38] The IR spectra of the complexes are given in Fig. S1.

The ^{1}H NMR spectrum of complex **1** shows a triplet at δ 3.55 ppm assigned to the dppm methylene protons, downfield shifted relative to free dppm (δ 2.77 ppm), confirming the phosphine coordination to the metal center. A sharp singlet at δ 4.76 ppm corresponds to benzyl protons, while multiplets at δ 7.23–7.60 ppm are attributed to aromatic protons (Fig. S2). In the $^{13}C\{^1H\}$ NMR spectrum, the benzyl carbon of the dithiocarbamate appears at δ 51.2 ppm, upfield shifted by ~5 ppm compared to the free ligand. Aromatic carbons resonate at δ 128–132 ppm, and the dithiocarbamate carbon appears at δ ~204 ppm with an upfield shift of ~7 ppm, consistent with coordination and π-delocalization over the NCS_2 moiety.

The $^{31}P\{^1H\}$ NMR spectrum displays a single resonance at δ −23.77 ppm, indicating equivalent phosphorus environments on the NMR timescale. However, the single crystal X-ray structure (*vide infra*) indicates a distorted square pyramidal geometry around the nickel center, with two dppm ligands bound in

Table 1 The physical properties of the complexes

Complex	Yield (%)	Melting point (°C)	Colour
1	~55	160–165	Brown
2	~83	240–245	Reddish-orange
3	~81	172–175	Reddish-orange

different modes (one bidentate and one monodentate) and one dithiocarbamate ligand (bidentate mode). This structural asymmetry would normally result in chemically distinct phosphorus environments and, consequently, multiple signals in the NMR spectrum. The observation of a single peak suggests a dynamic process in solution. This dynamic behaviour could involve a rapid exchange of the dppm ligands between the different binding modes, effectively averaging their environments and leading to a single averaged signal in the NMR spectrum at room temperature and even at −50 °C (Fig. S2). A similar phenomenon was reported by Puddephatt *et al.* for $[NiCl_2(dppm)_2]$ in solution, where a single peak was observed despite the presence of a distorted square pyramidal geometry in the solid state.[40] Therefore, while the solid-state structure provides valuable information, the $^{31}P\{^1H\}$ NMR data suggest a dynamic behavior in solution that renders a definitive assignment of the exact structure in solution difficult. Furthermore, a septet at $\delta \sim -144$ ppm in the $^{31}P\{^1H\}$ NMR spectra and a doublet at $\delta \sim -73$ ppm in the ^{19}F NMR spectra confirm the PF_6^- counter anion in the complex.

The ^1H NMR spectrum of complex **3** displays a triplet at δ 2.18 ppm and a singlet at δ 2.71 ppm assigned to the propylene protons of coordinated dppp, shifted relative to the free ligand (δ 2.16 and 1.58 ppm), confirming metal coordination. A sharp singlet at δ 4.59 ppm corresponds to the dithiocarbamate benzyl protons, while aromatic resonances appear at δ 7.10–7.60 ppm (Fig. S2). In the $^{13}C\{^1H\}$ NMR spectrum, the benzyl carbon resonates at δ 51.04 ppm, upfield shifted by ~5 ppm compared to the free ligand. Aromatic carbons are observed in the range of δ 127–133 ppm, and the dithiocarbamate carbon appears at δ ~204 ppm with an upfield shift of ~7 ppm, consistent with coordination and π delocalization over the NCS_2 unit. The $^{31}P\{^1H\}$ NMR spectrum of coordinated dppp shows a single resonance at δ 12.83 ppm, shifted from free dppp (δ −16.76 ppm), indicating a bidentate, chemically and magnetically equivalent coordination mode. The presence of the PF_6^- counterion is confirmed by a septet at $\delta \sim$ −144 ppm in the $^{31}P\{^1H\}$ NMR and a doublet at $\delta \sim -73$ ppm in the ^{19}F NMR spectrum. The spectroscopic parameters of related Ni complexes are summarized in Table S1.

Positive and negative ion mass spectrometry data were collected for complexes **1–3** to confirm their composition (Fig. S3). In the positive ion mode, a peak corresponding to $[M - dppm]^+$ was observed at m/z 714.1116 (30%) for complex **1**, whereas the peaks corresponding to $[M]^+$ were observed at m/z 728.1277 (100%) for complex **2** and 742.1426 (100%) for complex **3**. Furthermore, in the negative ion mode, complexes **1–3** exhibited molecular ion peaks at m/z 144.9644, which confirms the presence of the PF_6^- counter anion. These results validate that complexes **1–3** are ionic, consisting of a cationic Ni(II) species and a PF_6^- counterion.

X-ray structure of complexes 1 and 3

Single crystals of complexes **1** and **3** suitable for X-ray crystallography studies were obtained through the gradual evaporation of a dichloromethane/methanol solution of the complex mixture. Comprehensive crystallographic detailed molecular structure refinement details, as well as selected bond lengths and bond angles, are depicted in Tables S2 and S3, respectively. Complexes **1** and **3** crystallize in the triclinic system with the $P\bar{1}$ space group. Their molecular structures are illustrated in Fig. 2. The complexes showed distorted square pyramidal (**1**) and square planar geometries (**3**) around the Ni(II) center with one chelating dithiocarbamate S^S ligand and one P^P chelating diphenylphosphine ligand (dppm) and (dppp). For complex **1**, a monodentate dppm ligand completes the coordination sphere. In complex **3**, the root mean square (r.m.s.) deviation of four donor atoms (P1, P2, S1 and S2) in the equatorial plane from the least squares plane is 0.111 Å; however, the deviation of the nickel metal centre from the plane is −0.0568(7) Å. The distorted square pyramidal and square planar geometries around the nickel centre have also been supported by calculated geometrical index values (τ) of 0.375 and 0.129 in complexes **1** and **3**, respectively.[41] The Ni–S and

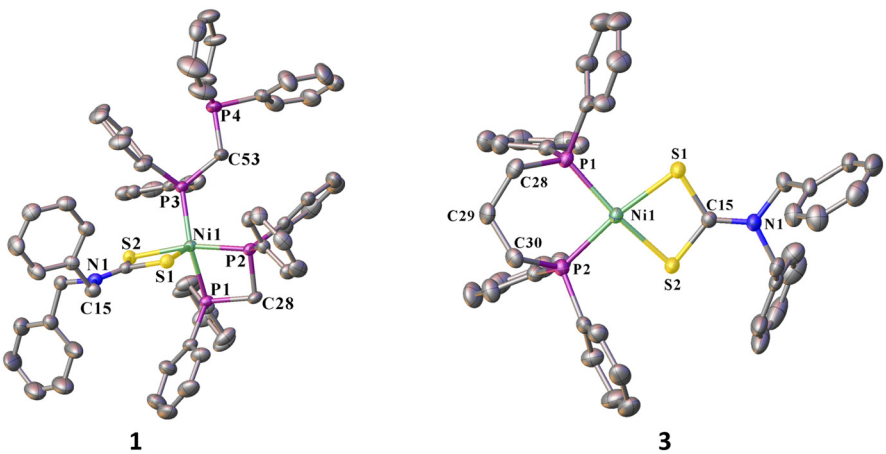

Fig. 2 ORTEP presentation of complexes **1** and **3** with ellipsoids shown at the 30% level. Hydrogen atoms, counterions, and solvent molecules are omitted for clarity.

Ni–P distances in complexes **1** and **3** fall within the ranges of 2.2135(10)–2.3895(9) Å and 2.1747(10)–2.2356(8) Å, respectively. In complexes **1** and **3**, the S(1)–Ni–S(2) bite angles are 76.13° (3) and 79.05° (4), respectively. These bite angles, significantly smaller than the ideal value of 90°, are due to the formation of the strained four-membered ring by chelating coordination of the 1,1-dithiocarbamate ligand. The P(1)–Ni–P (2) bite angle is 92.07(4) in complex **3**, which is larger than the ideal value of 90° due to the formation of a six-membered ring involving the dppp ligand. Furthermore, a comparison of selected bond lengths (Å) and bond angles (°) from analogous Ni-based complexes is given in Table S4.

The crystal structure of complex **3** shows Ni···H–C anagostic interactions with *ortho* protons of the dppp phenyl rings (2.98–3.08 Å, ∠C–H···Ni = 104.73–116.75°; Fig. S4). Weak intermolecular interactions (C–H···S, C–H···F, π···π) in complexes **1** and **3** direct the formation of one-dimensional supramolecular chains, with complex **1** forming C–H···S/π-stacked chains (Fig. S5) and complex **3** assembling *via* C–H···F hydrogen bonding (Fig. S6).

Electrochemical studies

Redox properties of the synthesized complexes. The redox behavior of complexes **1–3** was analyzed by recording the cyclic voltammograms (CVs) on a glassy carbon electrode in nitrogen-degassed dry acetonitrile (CH_3CN) containing 0.1 M $TBAPF_6$ as the supporting electrolyte and ferrocene (Fc) as an internal reference.[42] All the potential values are reported for Fc^+/Fc. The CVs of complexes **1–3** exhibit one-electron redox waves at $E_{1/2}$ = −1.39, −1.37, and −1.33 V, which correspond to the metal-centred $Ni^{II}(L)/Ni^{I}(L)$ redox process (Fig. 3a). The half wave potentials were obtained using differential pulse voltammetry (DPV), as shown in (Fig. S7). The cathodic peak currents (I_{pc}) corresponding to the Ni^{II}/Ni^{I} reduction for complexes **1–3** are observed at potentials (E_{pc}) of −1.44, −1.42, and −1.37 V and the anodic peak currents (I_{pa}), corresponding to the Ni^{I}/Ni^{II} oxidation of complexes **2** and **3**, are observed at potentials (E_{pa}) of −1.36 and −1.30 V *versus* $Fc^{+/0}$, respectively (Table 2). For the Ni(II)/Ni(I) redox wave, the peak-to-peak separation (ΔE_p) was found to be 60 mV and 70 mV for complexes **2** and **3**, respectively, indicating a one-electron transfer process according to the Nernst equation. This assignment is further supported by bulk chronocoulometric analysis of complex **3**, which also confirms a one-electron reduction process (Fig. S8a). The I_{pa}/I_{pc} values suggest that complex **3** undergoes a reversible and complex **2** a quasi-reversible redox process, whereas complex **1** exhibits an irreversible redox wave. The CV of the dithiocarbamate ligand suggests that the peak observed at potentials from −0.1 to −0.5 V is due to the electrochemical oxidation of the dithiocarbamate ligand (Fig. S8b). The linear correlation of peak currents of complexes **2** and **3** with the square root of scan rates revealed a diffusion-controlled electron transfer behaviour (Fig. S9), suggesting that the nickel complexes were fully dissolved and freely diffusing homogeneous species rather than adsorbing at the electrode surface or undergoing dissociation during the CV measurements. The diffusion coefficients for **2** and **3** are estimated to be 8.43×10^{-6} and 9.75×10^{-6} $cm^2\ s^{-1}$, respectively, from the slope of the peak current *versus* the square root of the scan rate plot, coupled with the Randles–Ševčík equation (eqn (S1)). The estimated values of diffusion coefficients are in line with the reported values of diffusion coefficients of similar-sized complexes.

Table 2 Comparison of redox properties of 1 mM of complexes **1–3** containing 0.1 M $TBAPF_6$ in acetonitrile at a scan rate of 100 mV s^{-1}

Complex	E_{pc}/V (Ni^{II}/Ni^{I})	E_{pa}/V (Ni^{I}/Ni^{II})	ΔE_p/V	$E_{1/2}$/V	I_{pa}/I_{pc}	D_{cat} ($cm^2\ s^{-1}$)	P–Ni–P bite angles
1	−1.44	—	—	−1.39	—	—	75.24(3)°
2	−1.42	−1.36	0.60	−1.37	0.57	8.43×10^{-6}	86.84(6)°
3	−1.37	−1.30	0.70	−1.33	0.88	9.75×10^{-6}	92.07(4)°

We observed that the complexes with larger chelate ring sizes demonstrated more positive reduction potentials. The crystal data show that the inclusion of the methylene groups in complexes **2** and **3** increases the chelate ring size with P–Ni–P bite angles of 86.84(6)° and 92.07(4)°, respectively, compared to 75.24(3)° in complex **1** with the dppm ligand. The chelate ring involving the dppp ligand in **3** forms a distorted chair form of a six-membered ring and has more spatial flexibility

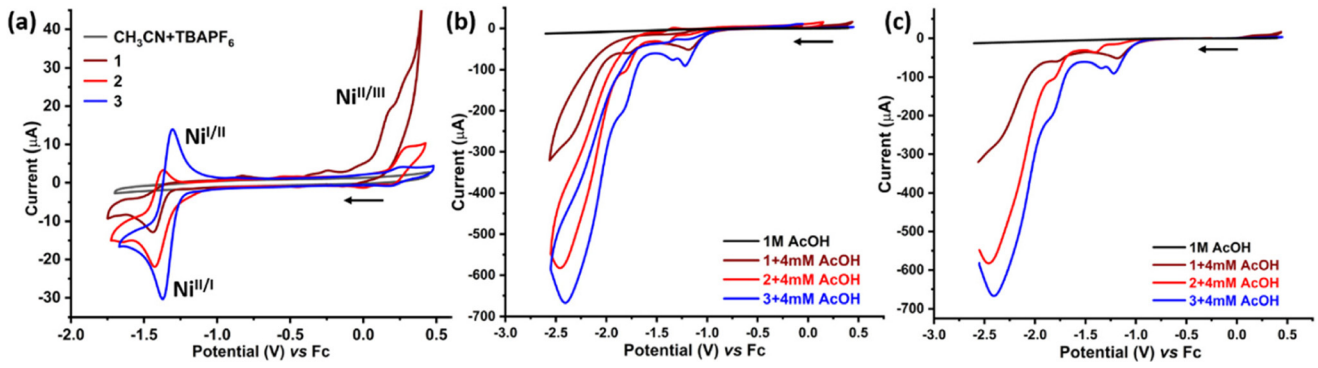

Fig. 3 Cyclic voltammograms (CVs) of 1 mM of complexes **1** (brown), **2** (red), and **3** (blue) in CH_3CN containing 0.1 M $TBAPF_6$ at a 100 mV s^{-1} scan rate: (a) in the absence of acid, (b) in the presence of 4 mM AcOH, and (c) linear scan voltammograms (LSVs) in 4 mM AcOH.

compared to the 4- and 5-membered chelate rings in **1** and **2**, respectively. The lower magnitude of the reduction potential of **3** indicates a reduced donor ability of the dppp ligand in **3** compared to the dppe ligand in **2** and dppm in **1**. This phenomenon is also supported by the NMR data.[43] The $^{31}P\{^{1}H\}$ NMR spectra of complexes **1–3** display a singlet at δ −23.77, 61.67, and 12.83 ppm, respectively, while free dppm, dppe, and dppp exhibit singlets at δ −21.77, −11.89, and −16.76 ppm, respectively. The change in the chemical shift value upon coordination to the metal center is 73.56 ppm in **2** and 29.59 ppm in **3**. The more downfield shift in **2** compared to **3** suggests relatively more donor ability of dppe in **2** compared to dppp in **3**. This makes the nickel center in complex **3** more electron-deficient and enables more facile reduction of Ni(II) to Ni(I) at the relatively lower (*i.e.*, less negative) potential. The variation of chelating ring size from 4 to 5-membered causes a small positive shift in the redox potential, ~20 mV ($\Delta E_{1/2}$). However, a more substantial positive shift of 40 mV is observed when the chelate ring size increases from a 5- to a 6-membered ring. The magnitude of the redox potential ($E°$) for $Ni^{II}(L)/Ni^{I}(L)$ of these complexes follows the trend **3** < **2** < **1** (Table 2), *i.e.*, with **3** exhibiting the most positive potential.

Furthermore, to establish which of the three complexes is the most robust and efficient HER catalyst, CVs and linear scan voltammograms (LSVs) were recorded in 4 mM acetic acid (AcOH) containing 1 mM of **1–3** with 0.1 M $TBAPF_6$ in CH_3CN at a 0.1 V s^{-1} scan rate (Fig. 3b and c). On the addition of acid, a broad wave appears around −2.3 V for complexes **1–3**. This wave was attributed to the catalytic wave for proton reduction. The enhanced electrocatalytic peaks at the more positive catalytic half-wave potential ($E_{cat/2}$) are observed for complexes **2** and **3**, whereas a weak catalytic peak at a more negative potential is observed for **1**. Therefore, complexes **2** and **3** were further analyzed as electrocatalysts for the proton reduction process.

Electrocatalytic hydrogen production

The electrocatalytic proton reduction by complexes **2** and **3** was further investigated using acetic acid, AcOH (pK_a = 23.51 in acetonitrile) as a proton source. The addition of AcOH results in the appearance of a new broad wave at around −2.4 V, which continues increasing with the subsequent addition of AcOH (Fig. 4). The new wave with $E_{cat/2}$ at −2.09 V (**2**) and −2.00 V (**3**), in 4 mM AcOH at a 100 mV s^{-1} scan rate, is attributed as the catalytic wave for electrochemical proton reduction. The addition of high acid results in a more negative shift of catalytic peak potential for both **2** and **3** (Fig. S10). The ratio of catalytic peak current in the presence (i_c) and absence of acid (i_p) is used to evaluate the performance of catalysts **2** and **3**. At low acid concentrations (<10 mM), the catalytic peak current increases linearly with increasing concentration of acid, which suggests first-order kinetics of the catalytic hydrogen evolution reaction concerning the acid concentration (Fig. 5a).

The catalytic peak becomes independent of acid concentration above 15 mM for complex **2** and 400 mM for complex **3** (Fig. 5a), indicating that the kinetics of the catalytic process are no longer limited by the acid concentration. Under such conditions, the i_c/i_p becomes independent of acid concentration and the scan rate. The limiting value of i_c/i_p indicates that the catalysts reach their maximum turnover frequency. Therefore, using this limiting i_c/i_p value from the experiment, the rate constant (k) for the hydrogen production process is estimated using the following mathematical relationship:[44]

$$\frac{i_c}{i_p} = \frac{n}{0.4463}\sqrt{\frac{RTk}{F\nu}} \quad (1)$$

where R is the universal gas constant, n (2 for HER) is the number of electrons transferred, T is the experimental temperature, F is Faraday's constant, and ν is the potential scan rate. The i_c/i_p value of 19.60 (**2**) and 60.32 (**3**) from Fig. 5a is

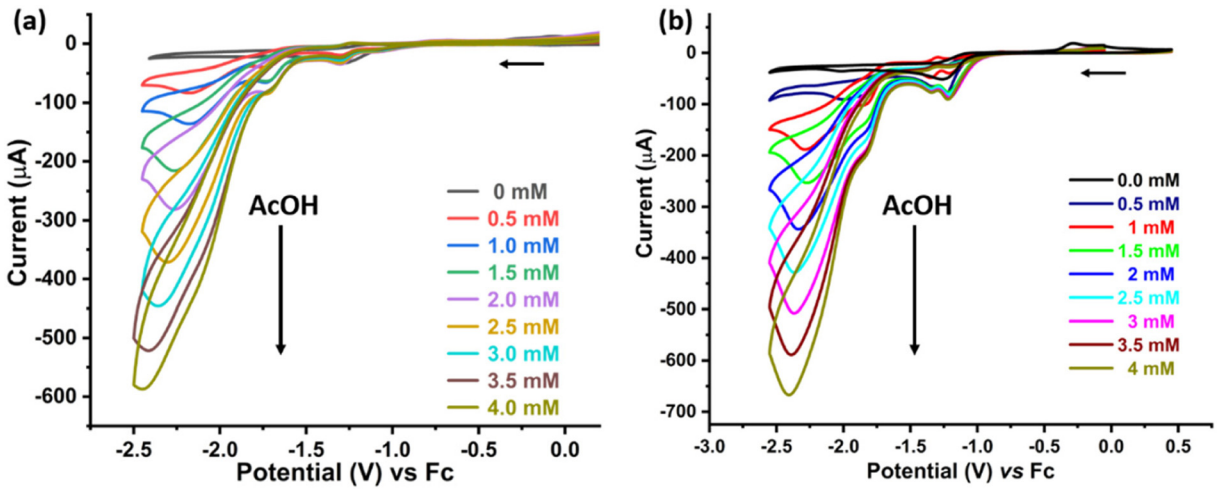

Fig. 4 (a) Cyclic voltammograms showing the variation in catalytic peak current with the subsequent addition of AcOH to the solution of 1 mM of complex **2** and (b) for complex **3** in CH_3CN containing 0.1 M $TBAPF_6$ at a 100 mV s^{-1} scan rate.

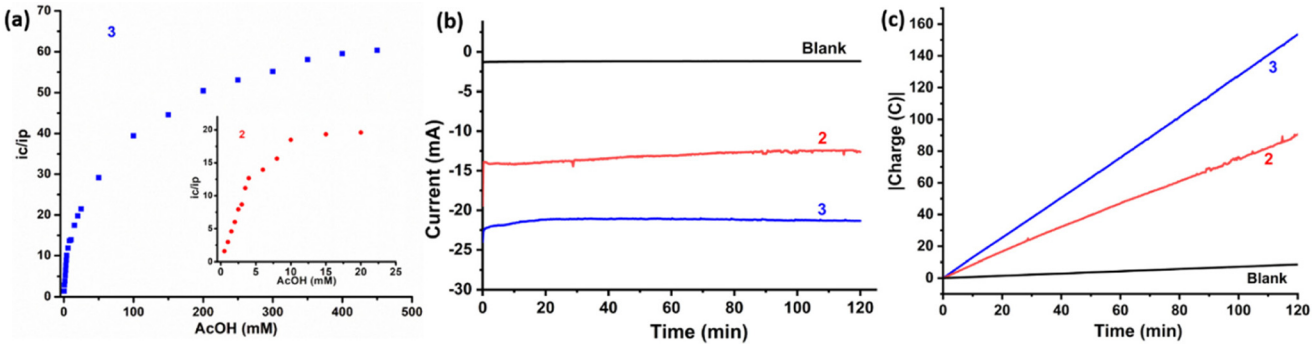

Fig. 5 (a) Plot showing the dependence of the relative catalytic peak current (i_c/i_p) on the increasing concentration of AcOH for complexes **2** and **3** at a 100 mV s^{-1} scan rate. (b) and (c) Plots showing the current and charge build-up *vs.* time in the constant potential electrolysis (CPE) experiment, recorded at −2.3 V *vs.* $Fc^{+/0}$ in 10 mL of acetonitrile solution containing 1 mM of complexes **2** and **3**, 500 mM AcOH and 0.1 M $TBAPF_6$. Blank experiments were performed under similar reaction conditions without a catalyst.

used to estimate the turnover frequencies (TOF) as 74.5 and 706 s^{-1} using eqn (1), respectively.

The overpotential (η) is another important characteristic parameter to evaluate the performance of catalysts. η is estimated by Appel and Helm's method and is determined using the following equation:[45]

$$\eta = \left|E_{cat/2} - E^{\circ}_{HA}\right| \quad (2)$$

where $E_{cat/2}$ is the catalytic half-wave potential and $E^{\circ}_{HA} = E^{\circ}_{H^+} - pK_a(HA)$. The theoretically observed $E^{\circ}_{H^+}$ is −0.028 V and pK_a is 23.51 for AcOH in acetonitrile. The thermodynamic potential E°_{HA} was determined to be −1.40 V.[46] The E°_{HA} value is also calculated using the Fourmond method at different acid concentrations.[45] In 4 mM of AcOH in CH_3CN, $E^{\circ}_{HA} = -1.33$ V *versus* $Fc^{+/0}$ (eqn (S2)). The overpotentials for **1–3** are obtained as 800, 690, and 600 mV, respectively. The CVs in Fig. 3a show a small difference in redox potentials, $\Delta E^{\circ} = |E^{\circ}(\mathbf{3}) - E^{\circ}(\mathbf{1})| = 60$ mV (*cf.* Table 2). This suggests that the electronic influence of the coordinated ligands is weak. On the other hand, the large difference in the catalytic half-wave potentials between complexes **1** and **3**, $\Delta E_{cat/2} = |E_{cat/2}(\mathbf{3}) - E_{cat/2}(\mathbf{1})| = 200$ mV from Table 3, can be attributed to the effect of chelating ligands. The catalytic activity of complexes follows the order of their P–Ni–P bite angles as 92.07(4)° (**3**) > 86.84 (6)° (**2**) > 75.24(3)° (**1**).

It is unlikely that the low overpotential and higher turnover frequency for complex **3** compared to **2** and **1** derive only from the electronic effects of coordinated ligands. Another reason for this difference is likely to be the spatial flexibility of the dppp ligand in **3** relative to the dppe ligand in **2**. The geometric fluctuations of the dppp ligand arise from the flexibility of the six-membered chelate ring, which can switch between chair and boat conformations. This enhances the entropic contribution, lowering the activation free energy barrier for proton reduction of complex **3**. Consequently, complex **3** is a more rapid and robust electrocatalyst for proton reduction than complexes **1** and **2**.

Table 3 Electrochemical characteristic properties of 1 mM of complexes **1–3** in 4 mM AcOH containing 0.1 M $TBAPF_6$ in CH_3CN at a 100 mV s^{-1} scan rate using a glassy carbon electrode. The faradaic efficiency (FE) was estimated using a graphite electrode

Complex	E^{onset}/V	$E_{cat/2}$/V	η/mV	i_c/i_p	TOF/s^{-1}	FE (%)
1	−0.81	−2.20	800	—	—	—
2	−0.92	−2.09	690	19.60	74.5	86.3
3	−0.98	−2.00	600	60.32	706	88.4

To test the stability of heteroleptic Ni(II) complexes (**2** and **3**) under electrocatalytic reaction conditions, standard rinse experiments were performed. The CVs recorded in AcOH before and after the electrocatalysis experiment exhibit no significant current variation or additional peak (Fig. S11). This ascertains the molecular integrity of the electrocatalysts and non-deposition of nano-particulate material on the surface of the glassy carbon working electrode during the electrochemical measurements. This stability is also confirmed by the UV-Vis spectra of the complexes, which show consistent peak characteristics and intensities in solutions after 4 hours of addition of 25 equivalents of AcOH (Fig. S12). The absence of spectral changes in the UV-Vis spectra with acid indicates that protonation of the complexes does not occur prior to electrochemical measurements.

To further obtain a significant amount of hydrogen evolution, we performed a constant potential electrolysis (CPE) experiment at a graphite electrode (6 mm diameter and 2 cm length) and in the presence of a high concentration (500 mM) of AcOH. The constant current with time, as shown in Fig. 5b, suggests the stability of complexes under reaction conditions and the absence of deposition of nano-particulate material on the electrode surface during bulk electrolysis. The identification and quantification of evolved hydrogen gas were obtained using gas chromatography (Fig. S13–S15). The obtained charge is directly proportional to the amount of H_2 generated per mole of catalyst and related to the turnover number and faradaic efficiency (FE) of the catalysts. The net amount of H_2 gas generated in a Tedlar bag by 1 mM of catalysts **2** and **3** in the presence of 500 mM AcOH was estimated

using a gas-tight syringe and obtained as 9.003 mL and 16.239 mL, respectively, after 2 h of CPE at −2.3 V. The faradaic efficiencies for H_2 production are obtained as 86.3% and 88.4% for **2** and **3**, respectively, and the detailed calculations, hydrogen peak area and GC report are provided in the SI. The physical characteristic parameters for the electrocatalysts are listed in Table 3. Moreover, complex **3** exhibited superior proton reduction activity compared to several previously reported Ni-based complexes (Table S5).

Mechanistic insights using spectroelectrochemical and computational analysis

A common mechanistic pathway observed for similar classes of Ni-based complexes is the ECEC mechanism[18,29,47–49] where E denotes an electron transfer and C signifies the chemical change due to H^+ binding. Initial ligand protonation inhibits the electron donation to Ni^{II}, facilitating the reduction of Ni^{II} to Ni^{I}, and consequently shifts the reduction potential to a less negative potential in the presence of an acid. The reduced Ni^{I}(L) complex further binds H^+ to form Ni(III)–H. Furthermore, identifying the rate-determining step is important for gaining mechanistic insight. Even in cases of rapid ET processes, kinetic limitations typically arise due to the slow first ($k_1 \ll k_2$) or second ($k_2 \ll k_1$) protonation step. For **2** and **3**, the $E_{cat/2}$ values are more negative than their E° (without AcOH), indicating that the first protonation step (k_1), leading to the formation of Ni^{III}–H, governs the rate-determining step. The ratio of k_1/k_2 (using eqn (S8)) for **2** and **3** is estimated to be 1.

Controlled-potential UV-Vis spectroelectrochemical measurements were performed in a 1 mM solution of complex **3** under a nitrogen atmosphere, applying potentials of −1.5 V (with 100 μL AcOH) and +0.7 V (without AcOH) (Fig. 6). Spectra were recorded at 10 min intervals over 50 min (Fig. S16). In general, the square planar Ni(II) dithiocarbamate complexes exhibit charge transfer bands in the spectral range of 300–450 nm and d–d transition bands occur in the region of ~450–800 nm.[18,26,36,50] It is interesting to note that upon applying a potential of −1.5 V in the presence of AcOH, a new charge transfer band appears at ~404 nm assigned to a ligand to metal charge transfer (LMCT) transition with additional absorption bands at ~436 and ~631 nm (Fig. S16a), which are characteristic of d–d transitions associated with the formation of a Ni(III)–H intermediate. The intensity of the absorption band at ~453 nm originally appeared in the spectrum of complex **3** decreases concurrently. Furthermore, an increase in the applied potential (−2.0 V) leads to hydrogen evolution and regeneration of complex **3** as indicated by the decrease in the intensity of the newly formed absorption bands. Moreover, the electrochemical oxidation of complex **3** at +0.7 V in the absence of acid results in absorption band characteristics of Ni(III) with LMCT bands at ~390 and ~400 nm along with d–d transition bands at ~438 and ~642 nm (Fig. S16b). These observations suggest that Ni(III)–H formation takes place under reductive conditions at −1.5 V in the presence of AcOH. Furthermore, TD-DFT calculations have been performed on the optimized structure of **3**, the Ni(III)–H intermediate C (Fig. 6b) and one electron oxidized species (Ni(III) species) (Fig. S17). The calculated absorption spectra for **3** and the Ni(III) intermediate show good correlation with the experimental data. Also, TD-DFT simulations of the proposed Ni(III)–H species reproduce key LMCT features between 350 and 400 nm and also a d–d transition at ~550 nm that are absent in the simulated spectrum of Ni(II) complex **3**. These computational results support the experimental findings and indicate the generation of the Ni(III)–H intermediate during electrochemical proton reduction. The chemically generated Ni(III)–H intermediate also exhibits a similar spectral band for d–d transition (~650 nm).[24]

Hydrogen gas release typically occurs *via* acid–base (heterolytic) or homolytic bimetallic routes, mainly controlled by ligand steric properties and acid/catalyst concentration.[51] The

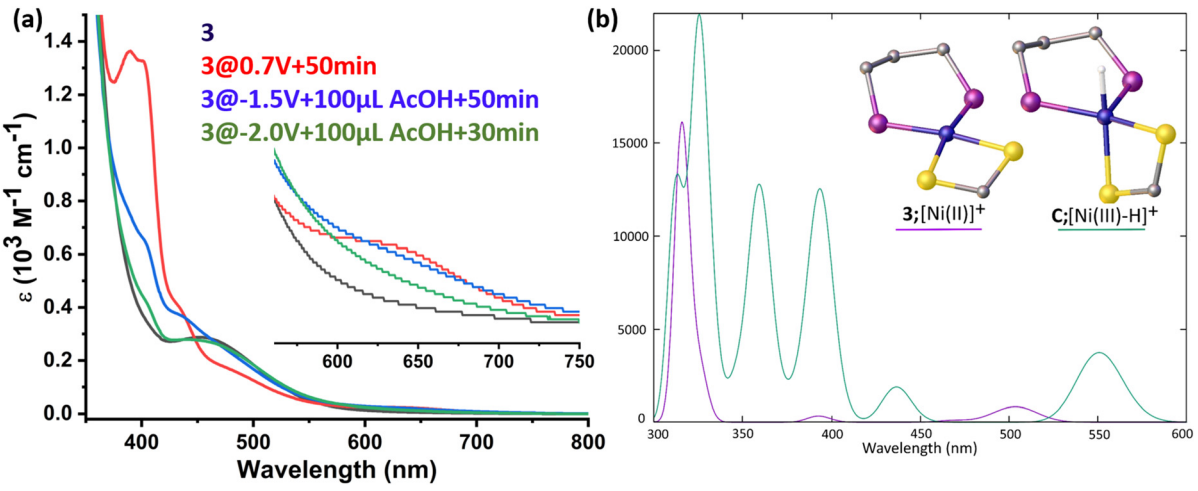

Fig. 6 (a) UV-Vis spectra of a 1 mM solution of complex **3** in CH_3CN containing 0.1 M $TBAPF_6$ recorded upon applying different potentials of +0.7 V (in the absence of AcOH) and −1.5 V and −2.0 V in the presence of 100 μL AcOH. (b) TD-DFT calculated absorption spectra of **3** and intermediate **C** (Ni(III)–H).

bulky phosphine-based ligands generally favour heterolytic HER over the homolytic pathways. The linear catalytic peak current variation with acid (in low acid concentration) in Fig. S18 and catalyst concentration in Fig. S19 supports the heterolytic pathway for H_2 production.[52,53] Furthermore, the detailed computational investigation of a plausible mechanism is discussed in the following section.

DFT calculations for the mechanism

To gain deeper insight into the HER mechanism of complexes **1–3**, DFT calculations were performed to elucidate the electrochemical/chemical pathways in correlation with experimental data (Scheme 2). The experimental observations indicate that a one-electron reduction of complex **3** precedes the rate-determining protonation step. The resulting one-electron reduced intermediate **A** exhibits a d^9 Ni center with one unpaired electron. This reduction (**3** → **A**) is exergonic (ΔG = −75 kcal) and accompanied by a conformational change from a square-planar geometry in **3** to a see-saw structure in **A**.

Since the CV scans of complexes **1–3** show no additional molecular reduction peaks beyond the Ni(II/I) couple, the subsequent step after reduction likely involves either direct protonation or a proton-coupled electron transfer (PCET) process. Spectroelectrochemical and TD-DFT results (Fig. 6) support the formation of a Ni(III)–H intermediate. To clarify its origin, we optimized protonated intermediates by placing the proton either on the Ni or S center of **A**. Both protonation pathways are endergonic, but protonation at the Ni center (ΔG = +29.5 kcal) is slightly more favorable than at the S center (ΔG = +30.6 kcal). The intermediate with S–H bonding is higher in energy and must proceed through a transition state (TS-BC, +10.2 kcal relative to **B**). Thus, direct protonation at Ni to form Ni(III)–H (**C**) is preferred. The pentacoordinate intermediate **C** adopts a distorted square-pyramidal geometry, with two S atoms, one hydride, and one P donor in the basal plane, and the other P atom occupying the apical position. The *in situ* formation of Ni(III)–H (**C**) is further supported by spectroelectrochemical studies (Fig. 6). Subsequent one-electron reduction of **C** to **D** (trigonal bipyramidal geometry) is highly exergonic (ΔG = −91.3 kcal), even more favourable than the initial reduction (ΔG = −75.0 kcal). Overall, this supports a PCET pathway (**A** → **D**), combining protonation followed by electron transfer, with a net exergonicity of −61.8 kcal, consistent with mechanisms proposed for other Ni–S-based HER catalysts.[16] For the second protonation, two configurations were examined: acetic acid hydrogen-bonded to the hydride ligand (**E**, +2.8 kcal) or to an S atom of the dithiocarbamate group (**E′**, +4.7 kcal). Attempts to locate a transition state analogous to the octahedral one reported by Jones *et al.*[29] were unsuccessful, suggesting a heterolytic HER mechanism.

The PCET pathway (**A** → **D**) inferred computationally aligns with electrochemical data. The metal-based peak intensity increases with increasing complex and acid concentrations, which can be attributed to proton-induced perturbation of the Ni(I) signal in the presence of acid (Fig. S19 and Fig. 3). To probe the PCET mechanism, we examined the effect of protons on the complexes in CH_3CN using UV-vis spectroscopy. The spectra of Ni(II) complexes **2** and **3** showed no noticeable changes upon addition of AcOH up to 25 mM (Fig. S12), indicating that protonation of the complexes does

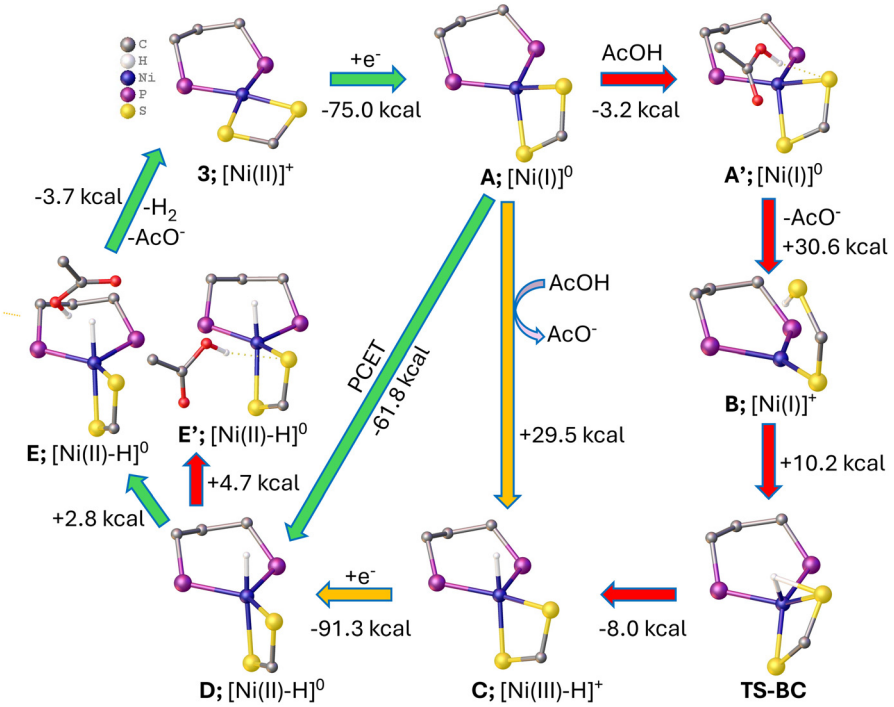

Scheme 2 Catalytic cycle for H_2 production by **3**. Only the immediate surroundings of the Ni centre are shown for clarity.

not occur under these conditions. To further investigate, we plotted the shift in the reduction peak potentials as a function of pH (Pourbaix diagram) in Fig. S20.[54] The first reduction wave corresponding to Ni(II/I) was largely unaffected while the newly formed wave shifted towards more positive potential with subsequent addition of AcOH from 1.5 to 4 mM. The result indicates that the proton concentration has a significant influence on further reduction of Ni(I) in the presence of acid. At low acid concentration (<3 mM), the slope of the second reduction peak is obtained as −54 mV pH^{-1}. This suggests that the protonation of Ni(I) is coupled with the electron transfer process, suggesting the coupling of middle CE steps in the ECEC mechanism, in accordance with the DFT results.

Experimental section

Materials and instrumentation

All experiments were conducted in the open air at ambient pressure and temperature. The solvents used in the synthesis were purified using established methods.[55] Reagent-grade chemicals, benzaldehyde (Qualigens), benzylamine (Avra), $NiCl_2{\cdot}6H_2O$ (Fisher Scientific), carbon disulfide, and THF (Merck), were used without additional purification. Dichloromethane and methanol solvents were distilled and purified using conventional procedures. The dithiocarbamate ligand was synthesized according to the previously reported procedure.[34,35,56] Melting points of complexes were determined in open capillaries using a Gallen Kamp apparatus and reported without correction. Infrared (IR) spectra (KBr pellet) were recorded on PerkinElmer IR instrument covering the range of 4000–400 cm^{-1} and multinuclear NMR spectra (^1H, $^{13}C\{^1H\}$, $^{31}P\{^1H\}$, and $^{19}F\{^1H\}$) were recorded in $CDCl_3$ solution on JEOL ECZ500 MHz NMR spectrometer. NMR chemical shift (δ) values are reported in ppm, and coupling constant (*J*) values are expressed in Hz. UV-visible absorption spectra of all complexes were acquired in CH_2Cl_2 solution using a Shimadzu UV-1800 instrument. Thin-layer chromatography (TLC) was performed on Merck 60 F254 silica gel plates pre-coated on an aluminium plate. Elemental analysis was performed using a vario MICRO CHNS analyser and mass spectrometric (MS) spectra were recorded on a SCIEX X500R (QTOF-MS) mass spectrometer. Cyclic voltammetry was carried out using the Metrohm Autolab M204 instrument in the presence of nitrogen gas at room temperature. The cell comprised a glassy carbon working electrode, a Pt wire auxiliary electrode, and Ag/$AgNO_3$ (10 mM) in CH_3CN containing 0.1 M $TBAPF_6$ as a reference electrode. Before utilization, the working GC electrode underwent a thorough cleaning process involving mechanical scrubbing with alumina powder of 0.5- and 0.03-micron particle sizes, along with subsequent sonication in ethanol and triple-distilled water for 15 minutes. Additionally, the Pt coil counter electrode was subjected to boiling in nitric acid in a temperature range of 45–50 °C for 10 minutes, followed by sonication in ethanol and triple-distilled water for 15 minutes each.[57] All measurements were conducted in acetonitrile (CH_3CN) with the addition of 0.1 M tetrabutylammonium hexafluorophosphate ($TBAPF_6$) as a supporting electrolyte. Ferrocene was introduced to each sample solution after the experiments, and the ferrocenium/ferrocene ($Fc^{+/0}$) redox couple served as an internal potential reference. Bulk electrolysis experiments were performed using graphite rods as the working electrode (6 mm diameter, 2 cm length), which were mechanically cleaned with 1500-grit emery paper, followed by sonication in ethanol and distilled water for 5 minutes each. The working electrodes (electrode 1 and electrode 2) were sealed at the same length in microtips to maintain a fixed area without leakage. The similarity in electrode areas was confirmed by nearly identical CV curves recorded in 0.1 M $TBAPF_6$ at a scan rate of 100 mV s^{-1} (Fig. S21). A Pt coil was used as the counter electrode. The gas generated during bulk electrolysis was analyzed using an Agilent 7890B gas chromatograph equipped with a thermal conductivity detector, using a PoraPak-Q column (for O_2 and N_2) and a molecular sieve column (for H_2).

Synthesis and characterization of complexes

The synthesis and characterization of complex **2** are reported in the literature.[58]

Complex 1. A solution of $NiCl_2{\cdot}6H_2O$ (0.118 g, 0.5 mmol) in 5 mL of methanol was mixed with a solution of dppm (0.192 g, 0.5 mmol) in 2 mL of dichloromethane, and the resulting reaction mixture was stirred for 30 min. Subsequently, a 10 mL methanolic solution containing the potassium salt of the dithiocarbamate ligand (0.155 g, 0.5 mmol) was slowly added, followed by the addition of NH_4PF_6 (0.81 g, 0.5 mmol) at RT. The reaction mixture was further stirred for 10 h. During this process, a brown-colored precipitate was formed, which was collected *via* filtration and washed with methanol (3 × 2 mL). Afterward, brown needle-shaped single crystals suitable for X-ray crystallographic studies were obtained by slow evaporation of a dichloromethane/methanol solution over two weeks at low temperature. Yield: 0.340 g (~55%). M.P.: 160–165 °C; ^1H NMR (500 MHz, $CDCl_3$ ppm): δ 7.61–7.56 (m, 16H), 7.42–7.39 (m, 30H), 7.24 (d, *J* = 8.0 Hz, 4H), 4.76 (s, 4H), 3.55 (s, 4H). $^{13}C\{^1H\}$ NMR (125 MHz, $CDCl_3$ ppm): δ 204.4, 132.8, 132.8, 132.7, 130.8, 129.4, 129.2, 129.1, 129.0, 128.6, 51.2, 31.2. $^{31}P\{^1H\}$ NMR (202 MHz, $CDCl_3$, ppm): δ −23.77, (Ph_2P–CH_2–PPh_2), 144.13 (sept, PF_6). ^{19}F NMR (470 MHz, $CDCl_3$ ppm): δ −72.58 (d, PF_6). UV–Vis. (CH_2Cl_2, λ_{max} (nm), ε (M^{-1} cm^{-1})): 310 (0.81×10^5). Anal. calcd for $C_{65}H_{58}F_6NNiP_5S_2$: C, 62.72; H, 4.70; N, 1.13%. Found: C, 61.23; H, 4.87; N, 1.23%. Positive ion ESI-MS: calcd for $C_{65}H_{58}NNiP_4S_2$: 1098.2315. Found: *m*/*z* [M − dppm]$^+$ 714.1116 (30%). Negative ion ESI-MS: calcd for PF_6^-: 144.9642. Found: *m*/*z* $[M]^-$ 144.9645, (100%).

Complex 3. This complex was synthesized using the procedure employed for the synthesis of complex **1**, from the dithiocarbamate ligand (0.155 g, 0.5 mmol), dppp (0.206 g, 0.5 mmol), NH_4PF_6 (0.81 g, 0.5 mmol), and $NiCl_2{\cdot}6H_2O$ (0.118 g, 0.5 mmol). Complex **3** was obtained as a reddish-orange precipitate, and reddish-orange needle-shaped single crystals suitable for X-ray diffraction analysis were obtained by

slow evaporation of dichloromethane/methanol solution at low temperature over two weeks. Yield: 0.360 g (~81%). M.P.: 172–175 °C; ^{1}H NMR (500 MHz, $CDCl_3$ ppm) δ 7.60 (s, 8H), 7.46–7.34 (m, 18H), 7.11 (d, J = 6.7 Hz, 4H), 4.59 (s, 4H), 2.71 (s, 4H), 2.18 (t, J = 25 Hz, 2H). ^{13}C{^{1}H} NMR (125 MHz, $CDCl_3$ ppm): δ 204.1, 133.0, 133.0, 132.9, 132.8, 131.7, 129.2, 129.2, 129.2, 128.9, 128.7, 127.6, 127.4, 127.2, 51.0, 23.1, 23.0, 22.9, 18.5. ^{31}P{^{1}H} NMR (202 MHz, $CDCl_3$, ppm): δ 12.83, (Ph_2P–CH_2–CH_2–CH_2–PPh_2), −144.02, (sept, PF_6). ^{19}F NMR (470 MHz, $CDCl_3$, ppm): δ −72.79 (d, PF_6). UV–Vis. (CH_2Cl_2, λ_{max} (nm), ε (M^{-1} cm^{-1}): 307 (0.64×10^5)). Anal. calcd for $C_{42}H_{40}F_6NNiP_3S_2$: C, 56.78; H, 4.54; N, 1.58%. Found: C, 48.17; H, 4.14; N, 2.39%. Positive ion ESI-MS: calcd for $C_{42}H_{40}NNiP_2S_2$: 742.1431. Found: m/z $[M]^+$ 742.1426 (100%). Negative ion ESI-MS: calcd for PF_6^-: 144.9642. Found: m/z $[M]^-$ 144.9640, (100%).

X-ray structure determination

Single crystal X-ray diffraction measurements were conducted for complexes **1** and **3** using a Rigaku SYNERGY XRD CCD diffractometer instrument and intensity data were collected under the illumination of graphite-monochromated CuKα (λ = 1.54184) for complex **1**, and Mo Kα radiation (λ = 0.71073 Å) for complex **3** at 298 K. Data integration and reduction were performed using the Chrysalis program.[59] Molecular structures were solved by using SHELXT[60] and refined using the SHELXL (2019)[61] program using X-Seed,[62] as the graphical interface. Diagrams representing the molecular structure of all complexes were generated using Mercury 3.8 and OLEX2-1.3.[50,63] The Crystallographic Data Centre (CCDC) reference numbers for complexes **1** and **3** are 2446704 and 2446705.

Computational details

DFT calculations have been performed using the ORCA 6.0.1 program package developed by Neese and co-workers.[64–66] The geometry optimization along with frequency calculations was carried out using the PBE0 functional with the def2-mTZVPP basis set reported with the r^{2}SCAN-3c composite functional.[67] Solvation effects in acetonitrile were included during all DFT calculations with the SMD solvation model.[68] Nudged Elastic Band (NEB) calculations were performed to locate the transition state **TS1**. IRC calculations were performed to confirm that transition states connect their respective intermediate species on both sides. For final energies, single point calculations were performed on r2Scan-3c optimized structures using PBE0 with larger basis sets (def2-TZVPP) on all atoms, and def2-ECPs on Ni, P and S were used for final single point energy calculations.[69] The energies obtained from single point calculations were converted to Gibbs free energies using the total corrections obtained for the thermochemical calculations following the frequency calculations at the smaller basis set level. Calculated Gibbs free energies were corrected for the standard state conversion from the gaseous state to 1 M solution at 298.15 K. To account for the entropy penalty during the change in the number of components during a chemical change, the MHP scheme[70] proposed by Martin, Hay, and Pratt was applied, which has also been used in several systems to produce reasonable results.[71–73] Changes in Gibbs free energies, ΔG, are reported in kcal mol^{-1}.

Summary and conclusions

This study reports the synthesis and characterization of three cationic heteroleptic Ni(II) dithiocarbamate complexes (**1–3**) bearing different diphosphine ligands (dppm, dppe, and dppp) and investigates the impact of their chelate ring size on electrocatalytic proton reduction. Single-crystal X-ray analysis revealed distorted square pyramidal (**1**) and square planar (**3**) geometries around the Ni(II) center. Notably, complex **3** exhibited intramolecular Ni···C–H agostic/preagostic interactions and formed 1-D polymeric chains *via* intermolecular C–H···F interactions in the solid state, while complex **1** displayed C–H···S and weak π···π stacking interactions also leading to 1-D polymeric networks. The diphosphine ligands (the dppm, dppe, and dppp) form four (**1**), five (**2**), and six-membered (**3**) chelate rings with increasing PNiP angles. The six-membered ring in **3** adopts a chair conformation in the solid state but is expected to exhibit conformational flexibility in solution. Electrochemical studies demonstrated that complex **3** displayed superior electrocatalytic hydrogen production in the presence of CH_3COOH, achieving a low overpotential (600 mV) and a high turnover frequency (~706 s^{-1}). The catalytic activity followed the order **3** > **2** > **1**, which is attributed to a combination of electronic effects from the diphosphine ligands and the enhanced flexibility of the larger chelate rings. The computational and spectroelectrochemical results suggest that the HER process occurs *via* the ECEC mechanism with the formation of Ni(III)–H as the rate determining step. Rinse and control potential experiments confirmed the stability of the complexes during catalysis. In conclusion, this work highlights the significant role of the diphosphine chelate ring size in modulating the electrocatalytic properties of these nickel complexes for proton reduction.

Author contributions

The manuscript was written through the contribution of all authors.

Conflicts of interest

The authors declare no competing financial interests.

Data availability

The data supporting this article have been included as part of the supplementary information (SI). Supplementary information: FT-IR, NMR, MS spectra of complexes, crystallographic details, additional CV data, bulk electrolysis, and computation

input coordinates in PDF format. See DOI: https://doi.org/10.1039/d5dt02840j.

CCDC 2446704 (**1**) and 2446705 (**3**) contain the supplementary crystallographic data for this paper.[74a,b]

Acknowledgements

We gratefully acknowledge financial support from the Banaras Hindu University–Seed Grant under the IoE Scheme (to Kamlesh Kumar) and the Swedish Research Council (to Ebbe Nordlander). Sarvesh Kumar Pal thanks the University Grants Commission (UGC), New Delhi, for SRF, and Anjali Mishra thanks the Council of Scientific and Industrial Research (CSIR), New Delhi, for providing the Senior Research Fellowship (SRF). The authors thank Kapil Bhati and the Central Instrumental Facility at the Indian Institute of Petroleum (IIP), Dehradun, India, for GC analysis.

References

1 G. W. Crabtree and M. S. Dresselhaus, *MRS Bull.*, 2008, **33**, 421–428.
2 M. Wang and F. Li, *Appl. Homog. Catal. Organometallic Compd. Handb*, 2017, pp. 1135–1194.
3 R. Das, F. Neese and M. van Gastel, *Phys. Chem. Chem. Phys.*, 2016, **18**, 24681–24692.
4 A. Kachmar, V. Vetere, P. Maldivi and A. A. Franco, *J. Phys. Chem. A*, 2010, **114**, 11861–11867.
5 H. Xu, J. Wan, H. Zhang, L. Fang, L. Liu, Z. Huang, J. Li, X. Gu and Y. Wang, *Adv. Energy Mater.*, 2018, **8**, 1800575.
6 H. Tang and M. B. Hall, *J. Am. Chem. Soc.*, 2017, **139**, 18065–18070.
7 G. Durgaprasad and S. K. Das, *J. Chem. Sci.*, 2015, **127**, 295–305.
8 J. K. Yadav, B. Singh, A. Mishra, S. K. Pal, N. Singh, P. Lama, A. Indra and K. Kumar, *Dalton Trans.*, 2024, **53**, 16747–16758.
9 J. K. Yadav, B. Singh, S. K. Pal, N. Singh, P. Lama, A. Indra and K. Kumar, *Dalton Trans.*, 2023, **52**, 936–946.
10 J. K. Yadav, A. Mishra, G. K. Mishra, S. K. Pal, K. U. Narvekar, A. Rahaman, N. Singh, P. Lama and K. Kumar, *New J. Chem.*, 2023, **47**, 20583–20593.
11 A. Z. Haddad, S. P. Cronin, M. S. Mashuta, R. M. Buchanan and C. A. Grapperhaus, *Inorg. Chem.*, 2017, **56**, 11254–11265.
12 P. Zhang, M. Wang, Y. Yang, T. Yao and L. Sun, *Angew. Chem.*, 2014, **126**, 14023–14027.
13 M. D. Sampson and C. P. Kubiak, *Inorg. Chem.*, 2015, **54**, 6674–6676.
14 D. Jana, H. K. Kolli, S. Sabnam and S. K. Das, *Chem. Commun.*, 2021, **57**, 9910–9913.
15 X.-L. Gu, J.-R. Li, Q.-L. Li, Y. Guo, X.-B. Jing, Z.-B. Chen and P.-H. Zhao, *J. Inorg. Biochem.*, 2021, **219**, 111449.
16 P. Saha, S. Amanullah and A. Dey, *J. Am. Chem. Soc.*, 2020, **142**, 17312–17317.
17 H. M. Tang and W. Y. Fan, *Inorg. Chem.*, 2021, **60**, 17933–17941.
18 A. Mishra, G. K. Mishra, N. Singh, R. Kant and K. Kumar, *Dalton Trans.*, 2024, **53**, 1680–1690.
19 C.-N. Lin, S.-T. Ren, L.-P. Ye, C.-H. Chen and S.-Z. Zhan, *Inorg. Chem. Commun.*, 2016, **69**, 24–27.
20 W. A. Hoffert, J. A. Roberts, R. M. Bullock and M. L. Helm, *Chem. Commun.*, 2013, **49**, 7767–7769.
21 R. M. Bullock, A. M. Appel and M. L. Helm, *Chem. Commun.*, 2014, **50**, 3125–3143.
22 S. Paul, S. Sutradhar, A. Paik, A. Biswas, S. Das, C. Das, R. Maity, A. Mahata, S. P. Midya, B. Maity and S. Rana, *Inorg. Chem.*, 2025, **64**, 7988–8000.
23 T. W. Tsega, D. T. Agub, S. D. Arco, C.-K. Chang and C.-H. Hung, *Inorg. Chem.*, 2025, **64**, 10792–10800.
24 N. X. Gu, P. H. Oyala and J. C. Peters, *J. Am. Chem. Soc.*, 2020, **142**, 7827–7835.
25 D. L. DuBois, *Inorg. Chem.*, 2014, **53**, 3935–3960.
26 M. Hirotsu, J. Sanou, T. Nakae, T. Matsunaga and I. Kinoshita, *Acta Crystallogr., Sect. E: Crystallogr. Commun.*, 2022, **78**, 500–505.
27 Y. X. C. Goh, H. M. Tang, W. L. J. Loke and W. Y. Fan, *Inorg. Chem.*, 2019, **58**, 12178–12183.
28 U. J. Kilgore, J. A. S. Roberts, D. H. Pool, A. M. Appel, M. P. Stewart, M. R. DuBois, W. G. Dougherty, W. S. Kassel, R. M. Bullock and D. L. DuBois, *J. Am. Chem. Soc.*, 2011, **133**, 5861.
29 L. Gan, T. L. Groy, P. Tarakeshwar, S. K. Mazinani, J. Shearer, V. Mujica and A. K. Jones, *J. Am. Chem. Soc.*, 2015, **137**, 1109–1115.
30 L. Chen, T. Li, B. Xie, C. Lai, R.-W. Ji, J.-Y. He, J.-X. Cao, M.-N. Liu, W. Li and D.-L. Zhang, *Catal. Sci. Technol.*, 2023, **13**, 3655–3666.
31 P.-H. Zhao, M.-Y. Hu, J.-R. Li, Y.-Z. Wang, B.-P. Lu, H.-F. Han and X.-F. Liu, *Electrochim. Acta*, 2020, **353**, 136615.
32 R. D. Hancock and L. J. Bartolotti, *Polyhedron*, 2013, **52**, 284–293.
33 A. Singh, K. Shiv, R. Singh, M. Bharty, P. P. Manna and L. B. Prasad, *Dalton Trans.*, 2024, **53**, 1196–1208.
34 S. K. Pal, B. Singh, J. K. Yadav, C. L. Yadav, M. G. Drew, N. Singh, A. Indra and K. Kumar, *Dalton Trans.*, 2022, **51**, 13003–13014.
35 Anamika, C. L. Yadav, M. G. Drew, K. Kumar and N. Singh, *Inorg. Chem.*, 2021, **60**, 6446–6462.
36 A. B. P. Lever, *Inorganic Electronic Spectroscopy*, 1968.
37 C. Carter, Y. Kratish, T. Jurca, Y. Gao and T. J. Marks, *J. Am. Chem. Soc.*, 2020, **142**, 18715–18729.
38 G. Hogarth, *Mini-Rev. Med. Chem.*, 2012, **12**, 1202–1215.
39 S. K. Singh, M. G. Drew and N. Singh, *CrystEngComm*, 2013, **15**, 10255–10265.
40 L. Manojlovic-Muir, H. A. Mirza, N. Sadiq and R. J. Puddephatt, *Inorg. Chem.*, 1993, **32**, 117–119.

41 L. Yang, D. R. Powell and R. P. Houser, *Dalton Trans.*, 2007, 955–964.
42 R. R. Gagne, C. A. Koval and G. C. Lisensky, *Inorg. Chem.*, 1980, **19**, 2854–2855.
43 H. V. Huynh, Y. Han, R. Jothibasu and J. A. Yang, *Organometallics*, 2009, **28**, 5395–5404.
44 V. C. C. Wang and B. A. Johnson, *ACS Catal.*, 2019, **9**, 7109–7123.
45 V. Fourmond, P. A. Jacques, M. Fontecave and V. Artero, *Inorg. Chem.*, 2010, **49**, 10338–10347.
46 A. Kütt, I. Leito, I. Kaljurand, L. Sooväli, V. M. Vlasov, L. M. Yagupolskii and I. A. Koppel, *J. Org. Chem.*, 2006, **71**, 2829–2838.
47 Q.-C. Chen, S. Fite, N. Fridman, B. Tumanskii, A. Mahammed and Z. Gross, *ACS Catal.*, 2022, **12**, 4310–4317.
48 R. Jain, A. A. Mamun, R. M. Buchanan, P. M. Kozlowski and C. A. Grapperhaus, *Inorg. Chem.*, 2018, **57**, 13486–13493.
49 M. Papadakis, A. Barrozo, T. Straistari, N. Queyriaux, A. Putri, J. Fize, M. Giorgi, M. Reglier, J. Massin, R. Hardre and M. Orio, *Dalton Trans.*, 2020, **49**, 5064–5073.
50 C. F. Macrae, I. J. Bruno, J. A. Chisholm, P. R. Edgington, P. McCabe, E. Pidcock, L. Rodriguez-Monge, R. Taylor, J. Streek and P. A. Wood, *J. Appl. Crystallogr.*, 2008, **41**, 466–470.
51 X. Guo, N. Wang, X. Li, Z. Zhang, J. Zhao, W. Ren, S. Ding, G. Xu, J. Li, U.-P. Apfel, W. Zhang and R. Cao, *Angew. Chem., Int. Ed.*, 2020, **59**, 8941–8946.
52 C. N. Valdez, J. L. Dempsey, B. S. Brunschwig, J. R. Winkler and H. B. Gray, *Proc. Natl. Acad. Sci.*, 2012, **109**, 15589–15593.
53 K. Kwak, W. Choi, Q. Tang, M. Kim, Y. Lee, D.-E. Jiang and D. Lee, *Nat. Commun.*, 2017, **8**, 14723.
54 D. Hong, Y. Tsukakoshi, H. Kotani, T. Ishizuka, K. Ohkubo, Y. Shiota, K. Yoshizawa, S. Fukuzumi and T. Kojima, *Inorg. Chem.*, 2018, **57**, 7180–7190.
55 B. S. Furniss, *Vogel's textbook of practical organic chemistry*, Pearson Education India, 1989.
56 Anamika, R. Singh, K. K. Manar, C. L. Yadav, A. Kumar, R. K. Singh, M. G. Drew and N. Singh, *New J. Chem.*, 2019, **43**, 16921–16931.
57 M. Kumar, G. K. Mishra and R. Kant, *Electrochim. Acta*, 2019, **327**, 135024.
58 S. K. Pal, T. Ansari, C. L. Yadav, N. Singh, P. Lama, A. Indra and K. Kumar, *Dalton Trans.*, 2025, **54**, 1597–1609.
59 *C. CrysAlis, RED, version 1.711. 13. J*, 1995.
60 G. M. Sheldrick, SHELXS-97, *Acta Crystallogr., Sect. A: Found. Crystallogr.*, 2008, **64**, 112–122.
61 G. Sheldrick, *Acta Crystallogr., Sect. C: Struct. Chem.*, 2015, **71**, 3–8.
62 L. J. Barbour, *J. Appl. Crystallogr.*, 2020, **53**, 1141–1146.
63 O. V. Dolomanov, L. J. Bourhis, R. J. Gildea, J. A. Howard and H. Puschmann, *J. Appl. Crystallogr.*, 2009, **42**, 339–341.
64 F. Neese, F. Wennmohs, U. Becker and C. Riplinger, *J. Chem. Phys.*, 2020, **152**, 224108.
65 F. Neese, *WIREs Comput. Mol. Sci.*, 2022, **12**, e1606.
66 F. Neese, *Wiley Interdiscip. Rev.:Comput. Mol. Sci.*, 2012, **2**, 73–78.
67 S. Grimme, A. Hansen, S. Ehlert and J.-M. Mewes, *J. Chem. Phys.*, 2021, **154**, 064103.
68 A. V. Marenich, C. J. Cramer and D. G. Truhlar, *J. Phys. Chem. B*, 2009, **113**, 6378–6396.
69 N. Mardirossian and M. Head-Gordon, *J. Phys. Chem.*, 2016, **144**, 214110.
70 R. L. Martin, P. J. Hay and L. R. Pratt, *J. Phys. Chem. A*, 1998, **102**, 3565–3573.
71 Y. Dang, S. Qu, J. W. Nelson, H. D. Pham, Z.-X. Wang and X. Wang, *J. Am. Chem. Soc.*, 2015, **137**, 2006–2014.
72 J. Zhang, Q. Zhang, Z. Zhu and B. Wang, *J. Organomet. Chem.*, 2020, **912**, 121173.
73 J. Ariai and U. Gellrich, *Phys. Chem. Chem. Phys.*, 2023, **25**, 14005–14015.
74 (*a*) CCDC 2446704: Experimental Crystal Structure Determination, 2026, DOI: 10.5517/ccdc.csd.cc2n3zyq; (*b*) CCDC 2446705: Experimental Crystal Structure Determination, 2026, DOI: 10.5517/ccdc.csd.cc2n3zzr.